Supplementary Information

Nanomaterial-Enhanced Molecular Recognition: A Co_3O_4/TiO_2 Heterojunction Electrochemical Sensor for Vanillin with Experimental and DFT Insights

Favour Ezinne Ogulewe, Akeem Adeyemi Oladipo*, Mustafa Gazi
Polymeric Materials Research Laboratory, Chemistry Department, Faculty of Arts and Science, TR North Cyprus, Eastern Mediterranean University, Famagusta via Mersin 10, Türkiye

S1. Data Analysis and Performance Metrics

S1.1. Electrochemically Active Surface Area (ECSA)

The electrochemically active surface area (ECSA, A, cm^2) of the modified and unmodified electrodes was estimated using the Randles–Ševčík equation for a reversible diffusion-controlled redox process:

$$I_p = (2.69 \times 10^5) n^{3/2} A D^{1/2} v^{1/2} \quad \text{(S1)}$$

where I_p (A) is the anodic or cathodic peak current, n is the number of electrons transferred, A is the electroactive surface area (cm^2), D is the diffusion coefficient of the redox probe ($cm^2 \cdot s^{-1}$), C is the bulk concentration ($mol \cdot cm^{-3}$), and v is the scan rate ($V \cdot s^{-1}$). Cyclic voltammograms were recorded in a 2.0 mM $[Fe(CN)_6]^{3-/4-}$ solution containing 0.1 M KCl at scan rates ranging from 10 to 200 $mV \cdot s^{-1}$. The linear relationship between I_p and $v^{1/2}$ confirmed diffusion-controlled electron transfer. For the $[Fe(CN)_6]^{3-/4-}$ redox couple, n=1 and the diffusion coefficient was taken as $D=7.6\times10^{-6}$ $cm^2 \cdot s^{-1}$. The slope of the Ip versus $v^{1/2}$ plot was used to calculate the ECSA of each electrode.

S1.2. Limit of Detection and Quantification

The analytical sensitivity of the sensor was evaluated by determining the limit of detection (LOD) and limit of quantification (LOQ) in accordance with IUPAC recommendations. These parameters were derived from the calibration curve using the following equations:

$$LOD = 3.3 \times (S_y/m) \quad \text{(S2)}$$

$$LOD = 10 \times (S_y/m) \quad \text{(S3)}$$

where S_γ is the standard deviation of the *y*-intercept of the regression line, and *m* is the slope of the calibration plot. Calibration curves were constructed using at least five concentration levels, each measured in triplicate.

S2. Calibration and Statistical Comparison with Reference Methods

S2.1. Calibration Strategy for Reference Methods

To benchmark the analytical performance of the proposed Co_3O_4/TiO_2-based electrochemical sensor, external calibration curves were established for both UV–Vis spectrophotometry and HPLC reference methods. Vanillin standard solutions spanning the concentration range encountered in real food samples were prepared in matrix-matched solvents. For UV–Vis analysis, absorbance at 280 nm was plotted against vanillin concentration, while HPLC calibration was based on peak area versus concentration. Linearity was assessed via least-squares regression, and LOD and LOQ values for the reference methods were calculated using Equations (S2) and (S3).

S2.2. Method Comparison and Statistical Validation

Quantitative results obtained using the electrochemical sensor (C_{sensor}) were statistically compared with those obtained by HPLC (C_{HPLC}) and UV–Vis (C_{UV-Vis}) for the same set of spiked real samples.

- **Relative Error (RE):** The initial assessment of analytical accuracy was conducted by calculating the relative error (RE):

$$\%RE = \left(\frac{C_{sensor} - C_{reference}}{C_{reference}}\right) \times 100$$

where $C_{reference}$ corresponds to either HPLC or UV–Vis results.

- **Paired *t*-Test (Accuracy Comparison):** A paired Student's *t*-test was performed at a 95% confidence level ($p < 0.05$) to evaluate whether statistically significant differences existed between the mean values obtained by the proposed sensor and the reference methods. The calculated *t*-value (t_{calc}) was compared with the critical tabulated value (t_{crit}) for the corresponding degrees of freedom. When $t_{calc} < t_{crit}$, the null hypothesis was accepted, indicating no statistically significant difference in accuracy between the methods.

- ***F*-Test (Precision Comparison):** The precision of the electrochemical sensor was compared with that of the reference methods using an *F*-test. The experimental *F*-value was calculated as the ratio of the variances of the two datasets. An experimental *F*-value lower than the critical *F*-value at the 95% confidence level indicated statistically comparable precision between the proposed sensor and the established analytical techniques.

For all evaluated samples (Table 1), the calculated *t*-values were lower than the critical *t*-value and the experimental *F*-values were below the tabulated *F*-values at the 95% confidence level, confirming statistically equivalent accuracy and precision.

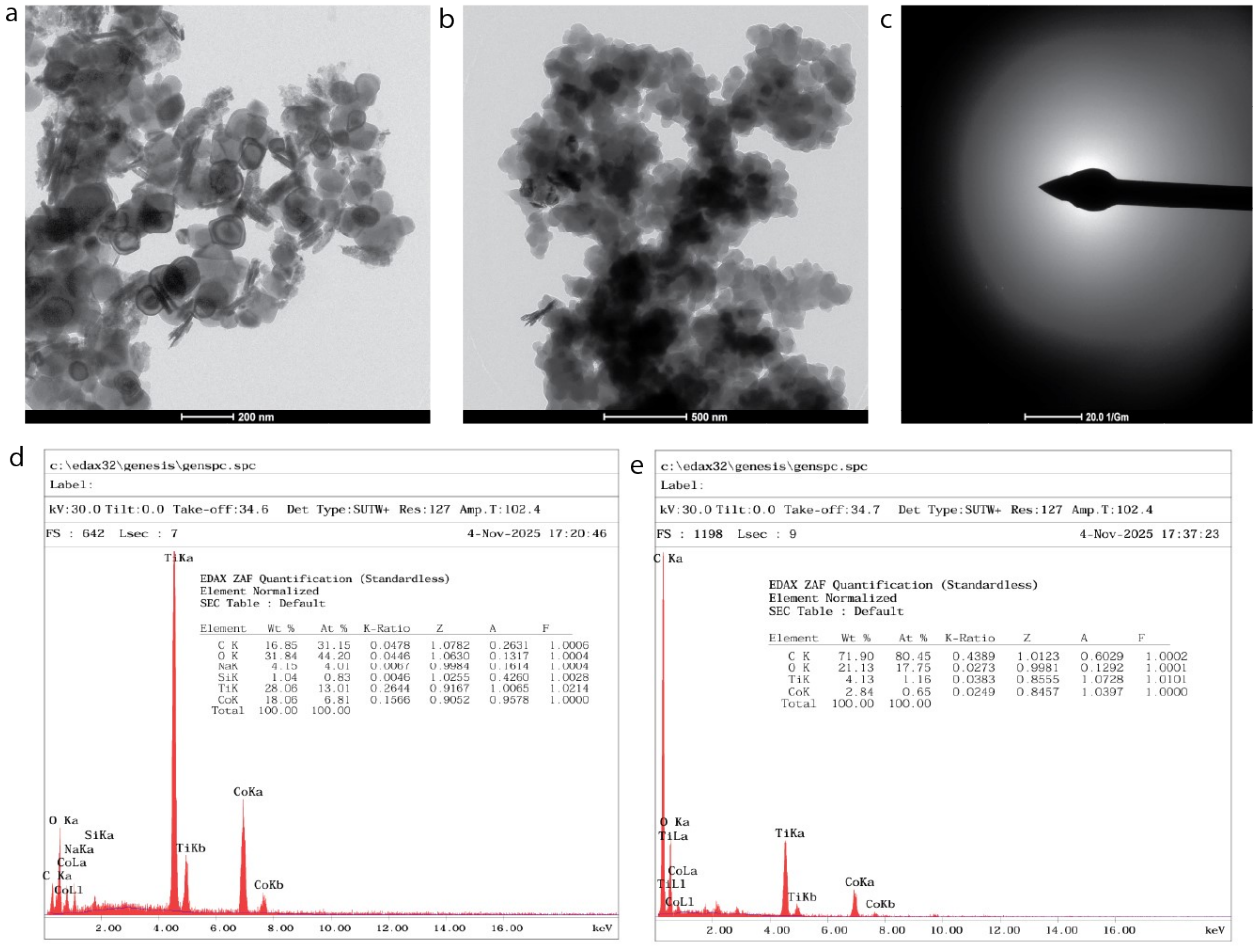

Fig.S1: a SEM image of Co_3O_4/TiO_2 **b** SEM image of MIP/Co_3O_4/TiO_2 **c** SAED pattern of MIP/Co_3O_4/TiO_2 **d** EDX of Co_3O_4/TiO_2 and **e** EDX of MIP/Co_3O_4/TiO_2

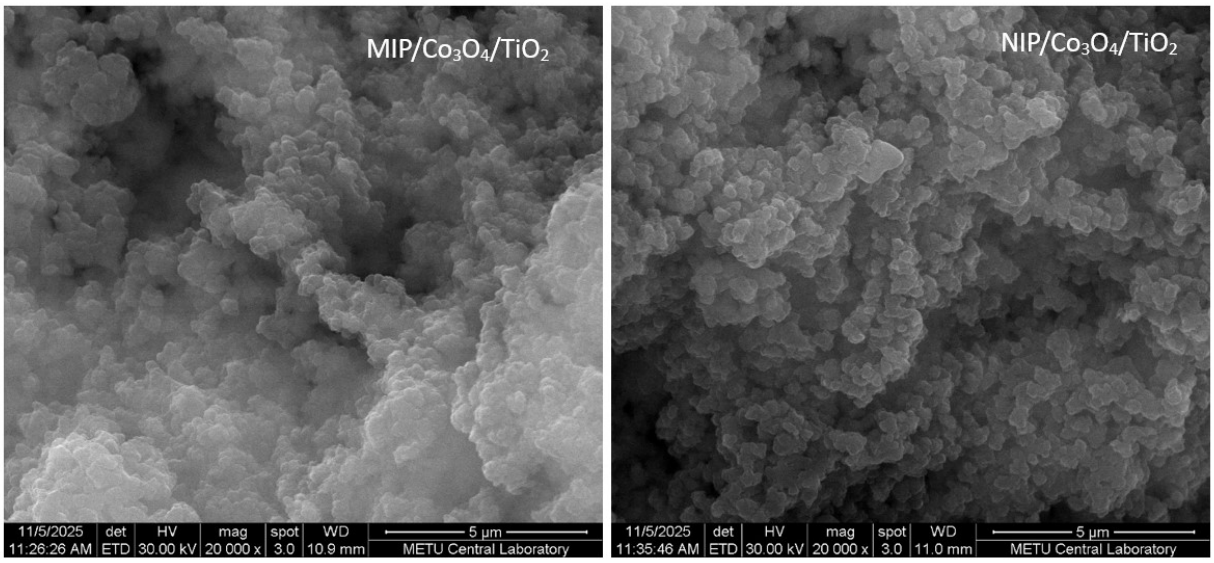

Fig.S2: SEM images of MIP/Co_3O_4/TiO_2 and NIP/Co_3O_4/TiO_2

S3. Electrochemical Characterization

The stepwise interfacial evolution of the modified electrodes was further examined by electrochemical impedance spectroscopy in the presence of the $[Fe(CN)_6]^{3-/4-}$ redox probe (Fig. S3). The Nyquist plots reveal a pronounced reduction in semicircle diameter upon Co_3O_4/TiO_2 modification, indicating substantially improved charge-transfer kinetics compared to the bare GCE. Introduction of the molecularly imprinted polymer slightly increased interfacial resistance while preserving efficient electron transport, whereas the non-imprinted polymer formed a more resistive interface, consistent with restricted redox accessibility. The corresponding Bode magnitude and phase plots further corroborate these trends, showing enhanced low-frequency impedance and altered phase behavior for the polymer-coated electrodes due to dielectric contributions from the polymer matrix. Additionally, the electroactive surface area (ECSA) for each electrode was determined from the linear dependence of anodic peak current (Ipa) on the square root of scan rate ($v^{1/2}$) using the Randles–Ševčík equation (Eq. S1), confirming that the

MIP architecture retains a significant fraction of the electroactive surface relative to the pristine nanocomposite.

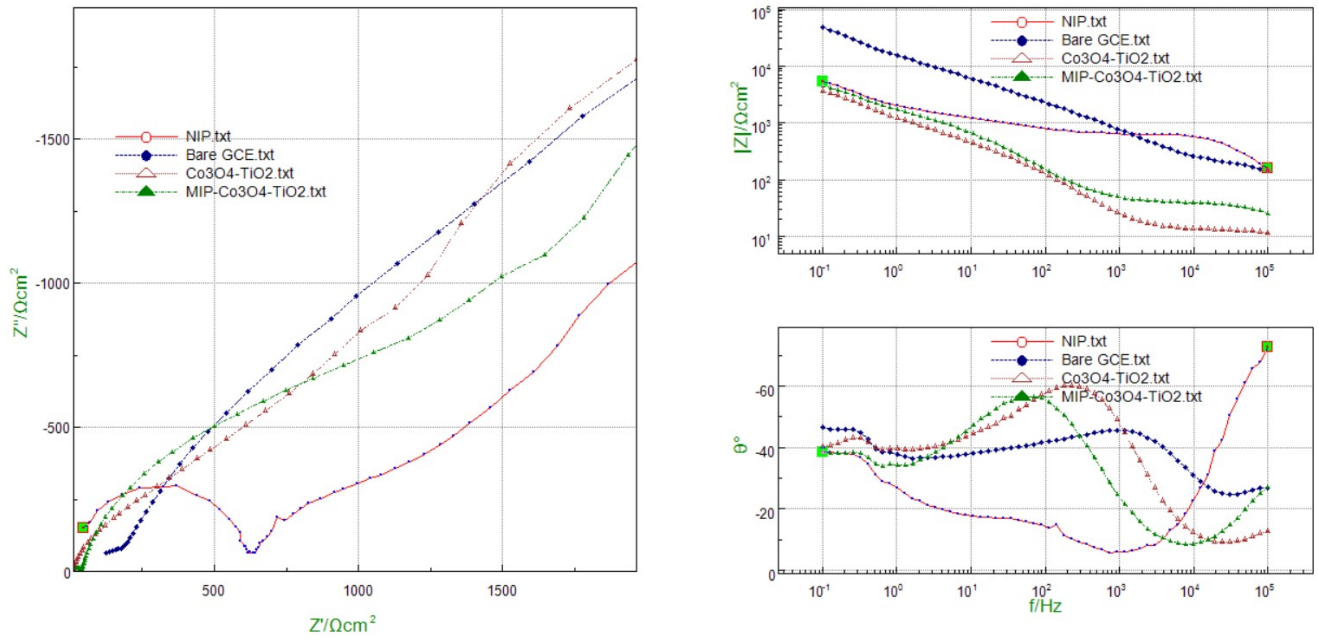

Fig.S3. Electrochemical impedance spectroscopy (EIS) characterization: Nyquist plots, Bode magnitude, and Bode phase plots for the bare GCE, Co_3O_4/TiO_2/GCE, MIP/Co_3O_4/TiO_2/GCE, and NIP electrodes. Measurements were recorded in 0.1 M KCl containing 2mM $[Fe(CN)_6]^{3-/4-}$.

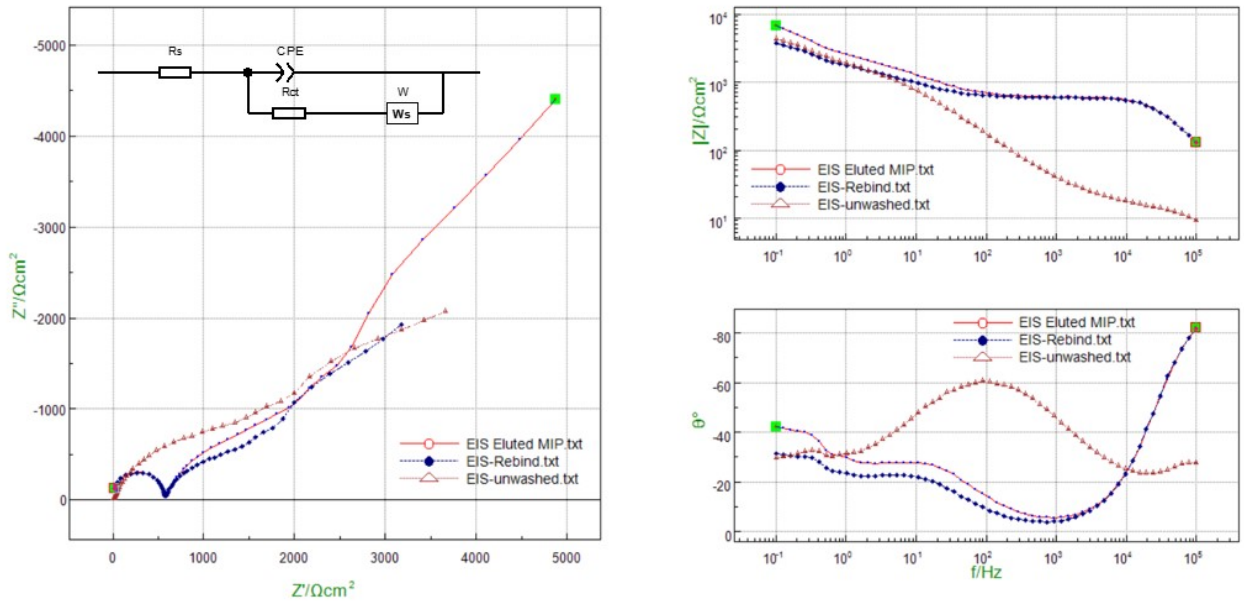

Fig. S4. Electrochemical impedance spectroscopy (EIS) characterization of the molecular imprinting and rebinding process. The figure presents the Nyquist plot (**left**) and corresponding Bode plots (**right**: impedance magnitude and phase angle) for the MIP/Co_3O_4/TiO_2 electrode at three distinct stages: the unwashed MIP (template embedded), the eluted MIP (after template extraction), and the rebound MIP (after re-incubation with vanillin). The significant decrease in impedance following elution confirms the successful removal of the template and the opening of conductive pathways, while the subsequent increase in impedance upon rebinding directly verifies the target-specific capture of vanillin within the imprinted cavities.

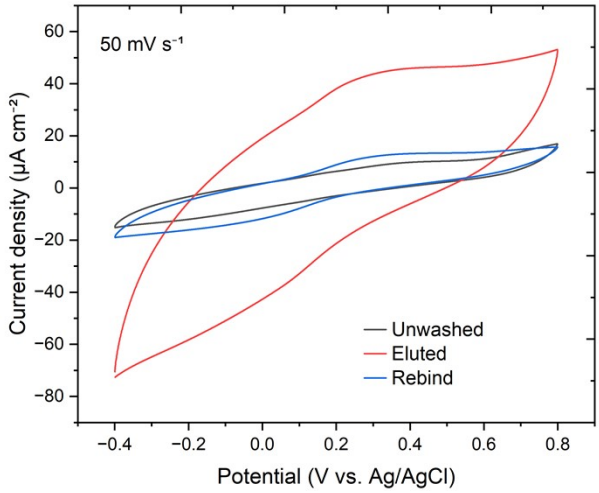

Fig.S5. Cyclic voltammetric evaluation of the molecular imprinting process. Voltammograms of the MIP/Co_3O_4/TiO_2 electrode are shown for the unwashed state (template embedded), the eluted state (after template extraction), and after rebinding with 25 μM vanillin. All measurements were recorded at a scan rate of 50 mV s^{-1}.

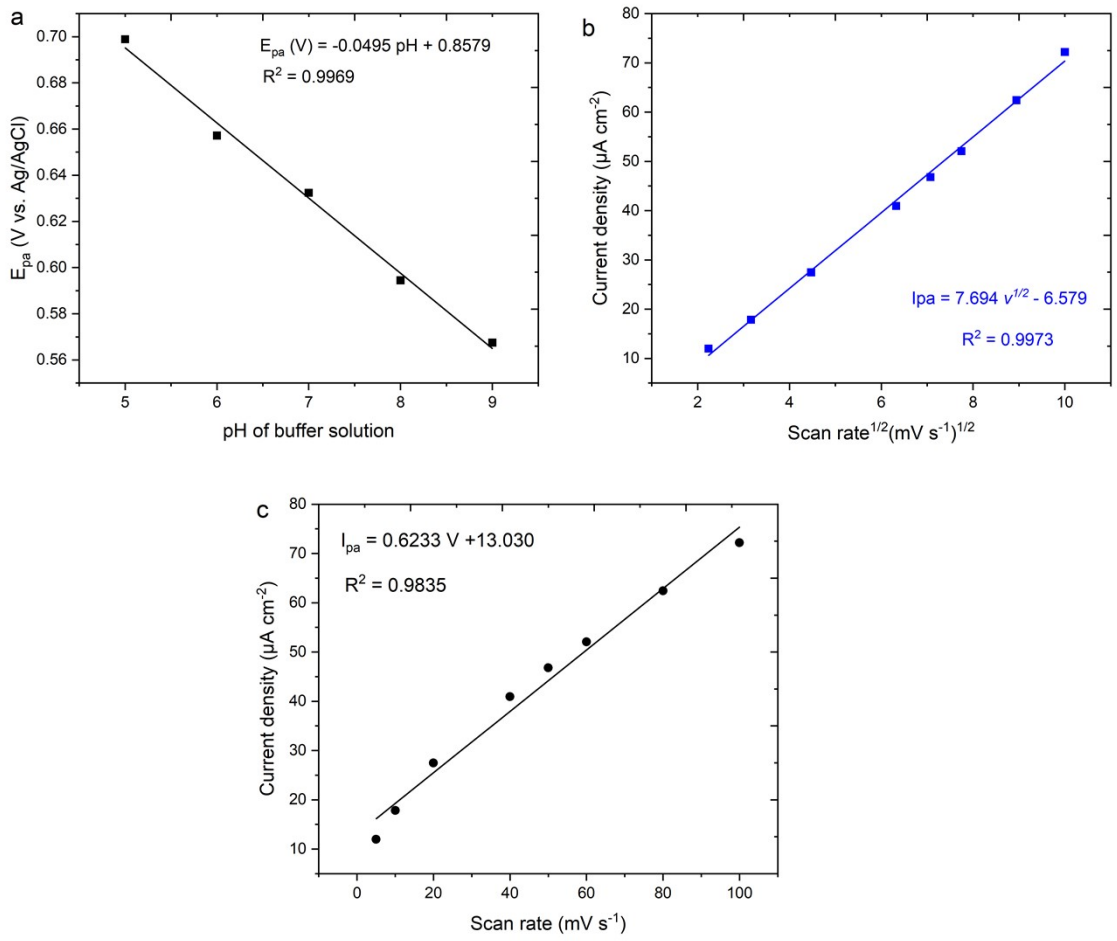

Fig.S6. a Dependence of oxidation peak potential on solution pH **b** square root of scan rate, confirming diffusion-controlled kinetics and **c** Linear relationships of anodic peak current with scan rate

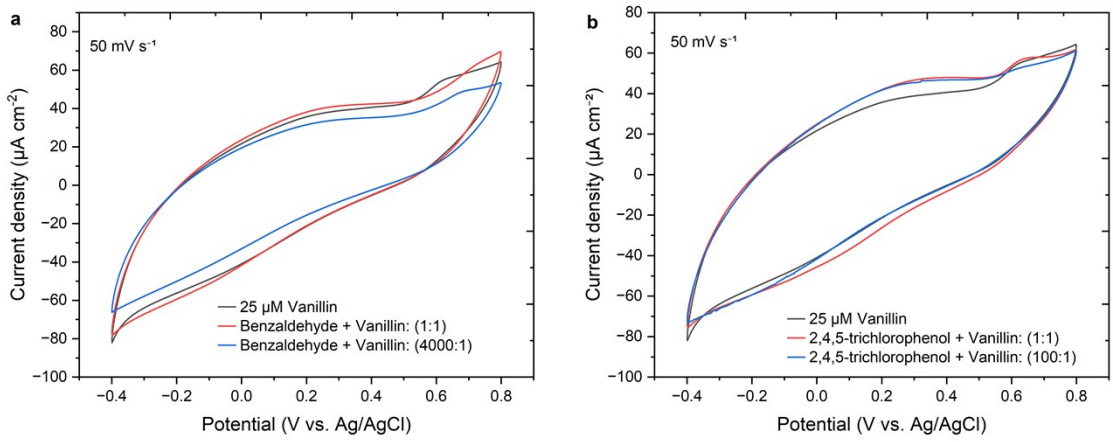

Fig.S7. Selectivity evaluation of the MIP/Co_3O_4/TiO_2 sensor against structural analogs and flavor additives. Cyclic voltammograms comparing the oxidation response of 25 μM vanillin alone to mixtures containing varying excess concentrations of (a) benzaldehyde and (b) 2,4,5-trichlorophenol. The preservation of the vanillin signal even at extreme interference ratios highlights the rigid steric and chemical specificity of the imprinted cavities.

S4. Comparative Binding Energy via DFT

The computational data (**Table S1**) predicts that the MIP designed for Vanillin have the highest affinity for its target. Ascorbic acid is a strong competitor (interference), while Glucose is unlikely to interfere significantly due to its weak binding.

Structural Drivers:

- **Vanillin:** The combination of the phenolic hydroxyl group, the aldehyde, and the methoxy group creates a "rigid" multi-point binding site. The aromatic ring also likely contributes π-π or π-dipole interactions with the acrylamide double bonds, stabilizing the complex further than H-bonding alone.
- **Ascorbic Acid:** While it has multiple -OH groups like Glucose, its planar, lactone ring structure allows for better geometric accessibility and stronger, more directional Hydrogen bonds than the flexible Glucose ring.

- **Glucose:** Despite having the most hydroxyl groups, its spatially bulky and flexible structure likely prevents the Acrylamide monomers from approaching closely enough to form a cooperative, high-energy network. The "quality" of H-bonds is lower here than in Vanillin.

DFT calculations at the PBE/DNP level reveal that Vanillin forms the most thermodynamically stable pre-polymerization complex with Acrylamide (ΔE = -28.49 kcal/mol). This strong interaction suggests the formation of high-fidelity imprinted cavities, superior to those formed by structural analogs like Ascorbic Acid (-20.23 kcal/mol) or Glucose (-12.57 kcal/mol).

Table S1: Comparative Binding Energy

Template	**$E_{complex}$ (Ha)**	**$\Sigma E_{monomers}$ (Ha)**	**ΔE (kcal/mol)**	**Selectivity Prediction**
Vanillin	-1276.351	-1276.306	**-28.49**	**Highest (Specific)**
Ascorbic Acid	-1423.535	-1423.502	**-20.23**	**Intermediate**
Glucose	-1352.935	-1352.915	**-12.57**	**Lowest (Non-Specific)**